Optical minibands in metallodielectric superlattices

N. Gibbons[*] and J. J. Baumberg

NanoPhotonics Centre, Cavendish Laboratory, University of Cambridge, Cambridge, CB3 0HE, United Kingdom
(Received 25 November 2011; published 11 April 2012)

Metallodielectric photonic crystals (MDBRs) display intriguing optical analogies to electronic transport phenomena in superlattices. The nearest-neighbor coupling between dielectric cavities leads to the formation of transmission minibands and minigaps. The properties of these optical Bloch modes are described in detail and related to the structural parameters of the MDBRs fabricated using a release-roll-up assembly technique. The angular and polarization dependencies of these miniband mode dispersion well matches transfer matrix simulations. As the cavity thicknesses are scaled down to <20 nm, these superlattices are predicted to exhibit metamaterial features based on the strongly anisotropic dielectric constant of the composite.

I. INTRODUCTION

Planar dielectric multilayers, also known as 1D photonic crystals, are commonly utilized as distributed Bragg reflectors (DBRs) and high-Q filters where their $\lambda/4$-thick layers lead to extremely high reflection coefficients across discrete frequency bands.[1] Semiconductor DBRs are commonly used in vertical-cavity surface-emitting lasers (VCSELs) and optical microcavities,[2] where light can be localized in a resonant $\lambda/2$ cavity layer. An interesting and subtly different structure can be achieved through similar principles by replacing one of the components with an ultrathin metallic layer ($\sim$10 nm). Unlike dielectric DBRs, metallodielectric DBRs (MDBRs) exhibit a stronger optical response due to the large refractive index contrast, δn, between metals and dielectrics. Consequently, only a few bilayers are required to produce significant Bragg resonances within the structure. In such configurations, the high reflectivity of the gold layers and their phase inversion removes the need for $\lambda/4$ layer thicknesses. In such Bragg-arranged configurations, resonant Fabry-Perot modes give rise to characteristic reflection and transmission bands. This allows such structures to act as transparent metals,[3,4] applicable in laser shielding, heat reflection ($R \approx 1$ across the entire infrared band) and in transparent conducting device technologies. This transparency also enhances their nonlinear properties: light can tunnel much deeper into such structures than the skin depth of the metal leading to a highly intensity-dependent refractive index (Kerr effect).[5–8] This makes such structures appealing as ultrafast optical switches, with potential also for second harmonic generation.[9] For all such applications, a detailed understanding of the role of nonuniformities on the optical properties, and their scalability with the number of layers, is important.

It is convenient to consider such metallodielectric photonic crystals as a series of coupled microcavites with the dielectric layers forming the cavities and the ultrathin metallic layers acting as the mirrors. The coupling between the cavity modes causes their degeneracy to split and form transmission minibands, each separated by a photonic band gap (minigap).[12] Viewed from this perspective, the coupling of the cavity modes is analogous to the tight-binding theory of atomic orbitals within a lattice.[10,11] Furthermore, the optical analogues of Bloch oscillations and Zener tunneling can be drawn from this comparison. While in a semiconductor crystal, Bloch oscillations arise from the introduction of an external electric field along the direction of electron propagation, their optical analog can be achieved by imposing a gradient in the resonant cavity frequency parallel to the direction of light propagation. This can be achieved by changing the optical thickness of the cavity layers, through either their refractive index or cavity layer thickness. This leads to coupling between the transmission minibands and a spatial tilting of the photonic band gap. The photonic states of the coupled cavity structure split into a series of discrete energy levels, analogous to the electronic Wannier-Stark ladder (WSL).[12] At a critical gradient, delocalization of these WSL energy levels occurs, leading to resonant tunneling through the structure. This sharp transmission resonance is comparable to the electronic phenomenon of Zener tunneling in a semiconductor superlattice.[13]

The use of plasmonic metals in such periodic structures leads to imaging applications. It was originally proposed that a single silver slab could act as a "perfect lens" by focusing light through negative refraction and crucially, amplifying the evanescent modes of an image.[14] These high-k components decay exponentially and are normally lost from an image but they are able to couple to the surface plasmons (SPs) residing on the silver surface, thus allowing propagation and refocussing. The huge losses in a bulk metallic layer are unavoidable, however, and an improvement was suggested based upon a series of ultrathin metallic layers separated by a dielectric spacer.[15] Below the plasma frequency ω_p, the electric permittivity ϵ undergoes a change in sign between the metallic and the dielectric layers and so propagating light undergoes alternate positive and negative refraction. The light is prevented from ever reaching extremely high amplitudes within the structure and losses are greatly reduced. At small enough dimensions (subwavelength) the layers can be considered part of an effective medium[16] with well defined optical properties. Consequently ϵ becomes anisotropic,[17] being negative along the plane of the layers and positive in the normal direction. This effect has since been exploited in the successful fabrication of a number of functioning superlenses and hyperlenses[18–20] achieving resolution down to $\lambda/20$. In such configurations, the evanescent modes contribute to the enhanced resolution, however, subwavelength imaging has also been demonstrated using only propagating modes in a Bragg-arranged structure.[21]
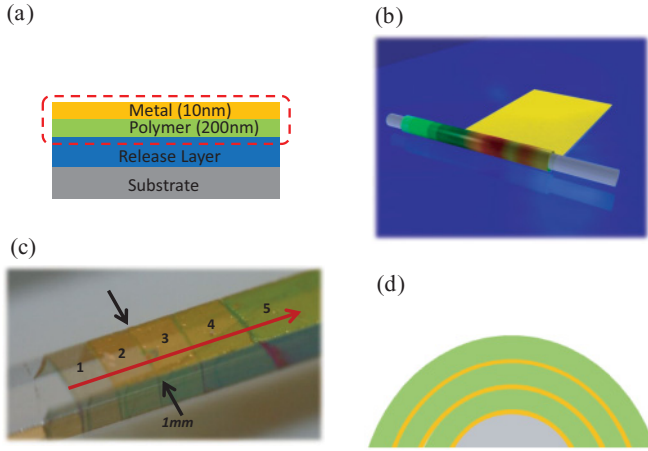
FIG. 1. (Color online) (a) Bilayer structure before roll up. (b) Film is floated from substrate and rolled up around glass rod ($d = 1$ mm). (c) Sample image showing different numbers of bilayers along the rod axis. (d) Cross section of sample.

In this paper, we discuss in detail the nature and origin of the optical resonances in the Bragg regime and in the metamaterial configuration. The MDBRs discussed here are flat, helically rolled and comprise of up to 12 bilayers of polydimethylsiloxane (PDMS), a commercial elastomer with refractive index $n = 1.41$ and approximately 10 nm of gold (Fig. 1). They were fabricated by release roll-up assembly (RRA) in which a single bilayer is rolled[4] around a central rod to form a multilayer, or by folding methods.[26] With this approach, multilayers can be effectively fabricated with large area, few defects and with a large number of layers ($\geqslant 100$). Due to the helicity of the samples, different numbers of layers can be optically accessed along the axis of the central rod. Details of sample fabrication can be found in previous papers.[4] Here we show detailed spectroscopy into the near infrared (NIR) of such miniband modes and discuss the factors that control their linewidth and transmissivity.

II. FABRY-PEROT RESONANCES

Reflection and transmission spectra are taken from successive points along the axis of the sample with an increasing number of layers. A modified fibre-coupled microscope with a spot size of 25 μm is used in conjunction with two spectrometers (visible and NIR) covering simultaneously a wavelength range between 400 and 1600 nm. Typical spectra are displayed in Fig. 2 along with corresponding fitted simulations for 4, 8, and 12 bilayers of the sample. The simulations are produced using standard multilayer calculations based on the impedance method,[22] which has better stability for such multilayer metallic structures. The distinct stopband (shaded in blue) and sharp, fundamental Bragg resonances develop as the number of layers increases. The number of Bloch modes in the transmission miniband, $M = L - 1$, where L is the number of bilayers. Toward the NIR the reflection rises to ≈ 1 with the transmission and absorption dropping to zero. Due to the high contrast between n_{Au} and n_{PDMS} between 400 and 1000 nm ($\Delta n > 1$), the resonances are sharper than those found in a purely dielectric stack. The stopband itself is also shaped
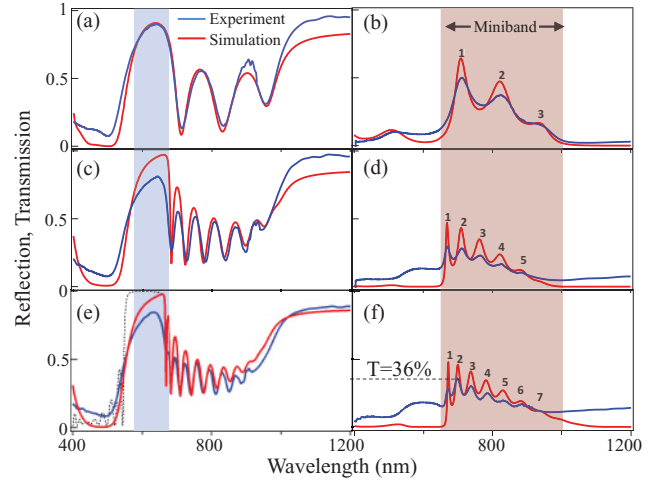

FIG. 2. (Color online) Reflection spectra (red: simulated, blue: experimental) of (a) 4, (c) 8, and (e) 12 bilayers. Photonic band gap is shaded. Equivalent symmetrical stopband for a purely dielectric DBR is also shown for 12 layers in (c) (dashed line). Transmission spectra for the same positions with (b) 4, (d) 8, and (f) 12 bilayers. Transmission miniband is shaded.

differently to that of a dielectric DBR, becoming triangular and dropping off sharply toward 500 nm. For comparison, the stopband resulting from a 12 bilayer polymer/air DBR is shown in Fig. 2(e) (dashed line). This effect arises from the spatial distribution of the optical field within the gold layers. At the short λ side of the stopband, higher field intensities sit within the gold leading to a sharp rise in absorption. Field distributions within the samples are discussed in more detail below. These optical resonances are highly sensitive to dielectric and gold layer thicknesses and can be easily shifted across the entire visible and NIR spectrum. The wavelength of the stopband center is approximately twice the PDMS thickness, t_{PDMS}. The gold layers must be close to the skin depth (≈ 20 nm when $\lambda = 500$ nm). Despite a total thickness 24 times larger than the skin depth, 36% transmission can be experimentally achieved with 12 bilayers [see Fig. 2(f)].

The dispersion relation of this structure can be experimentally extracted from the miniband Bloch mode positions. The frequency of the modes is found from the dip positions in the reflection spectra [see Fig. 3(a)] and their momentum is
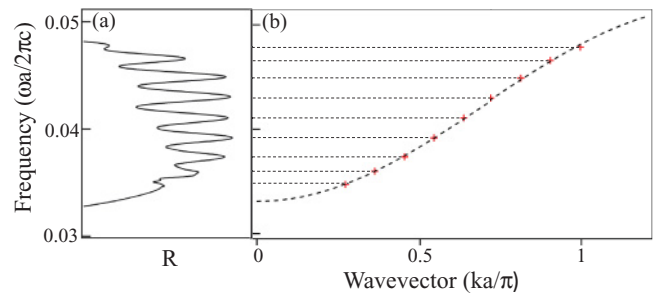

FIG. 3. (Color online) (a) Miniband Bloch mode positions in frequency. (b) Experimental dispersion relation of 12 bilayers from the first nine miniband modes ($+$).

derived from the periodicity of the structure, $k_N = \frac{\pi}{a}(\frac{M-N}{M-1})$, where a is the optical lattice constant of the multilayer, N is the miniband Bloch mode number and $M = 11$, is the total number of Bloch modes. The dispersion relation of the superlattice is controlled by the thickness and refractive index of the spacer layers and the coupling between each dielectric cavity layer and is given from tight-binding theory to be[23]

$$\omega(k) = \Omega[1 + \kappa \cos(ka)], \qquad (1)$$

where $\kappa = \beta - \alpha$ is a tight-binding parameter that describes the degree of coupling between two cavities and is found from the miniband mode splitting for two coupled cavities:

$$\omega_{1,2} = \Omega\sqrt{\frac{(1 \pm \beta)}{(1 \pm \alpha)}} \qquad (2)$$

with Ω being the central frequency of the miniband.

Physically, the cavity coupling constant κ is dependent on the photon transmission probability through one metallic layer. For the experimental parameters used here, the miniband indeed has the familiar form arising from dominant nearest-neighbor coupling.

III. LAYER DISORDER

The quality factor, $Q = \lambda/\Delta\lambda$, of each successive dip drops exponentially as shown in Fig. 4, flattening out at higher mode numbers. Comparing experimental and simulated spectra shows a lower than expected Q observed experimentally for the lower-λ modes. Simulating the properties of these structures using perfectly periodic (PP) layers is inappropriate since even low levels of disorder within the layers influence the shape and position of the resonances. This is illustrated in Fig. 5 where reflection and transmission spectra are contrasted with both PP fits and optimized fits that include disorder in both the polymer and gold layers. In these improved simulations, each layer thickness has an additional Gaussian distributed variance of specific width δ_i. The roughness adopted for these optimized fits is supported by AFM measurements of the initial bilayers. Simulated spectra then average over 100 configurations of differently disordered structures, which is acceptable since the lateral scale of the disorder is much smaller than the probed spot size in these measurements.

To understand the influence of disorder more clearly, the individual effect of gold and polymer disorder of different magnitudes are compared in Fig. 6. First, the polymer disorder
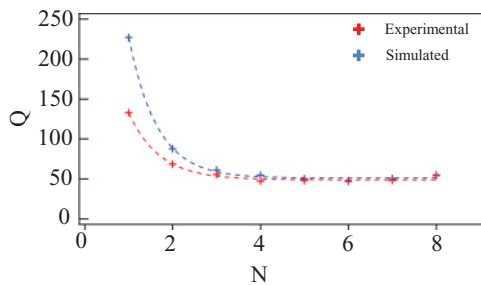
FIG. 4. (Color online) Extracted Q factor of the first eight Bloch modes from a 12 bilayer sample. Experimental (red) and simulations (blue).
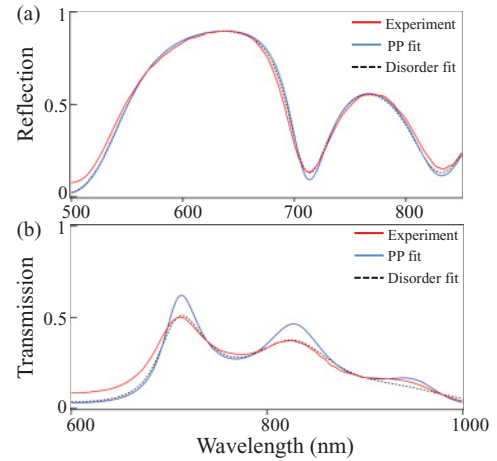
FIG. 5. (Color online) (a) Reflection spectra of four bilayers: experimental (red), perfectly-periodic simulation (blue), and optimum fit with polymer disorder, $\delta_p = 3$ nm and metal disorder, $\delta_m = 0.5$ nm, within each bilayer. (b) Transmission spectra fitted with same parameters.

δ_p is varied between 1 and 4 nm and the resulting spectra are plotted alongside the PP simulation [see Fig. 6(a)]. In the case of a PP structure, miniband Bloch modes arise from the constructive interference between the gold mirrors and the subsequent coupling between these degenerate cavity modes. As δ_p is increased, the resonant condition is altered for each successive cavity and thus destructive interference is increased. The direct effect of this is to reduce the Q of each miniband mode. An additional effect of this layer disorder is a slight red-shift ($\approx$1 nm) of the mode position. While the individual spectra either blue shift (from reductions in thickness) or redshift (increases in thickness), the magnitude is asymmetric. This leads to an asymmetrical shift around the original mode position and a net redshift in the spectra of the disordered
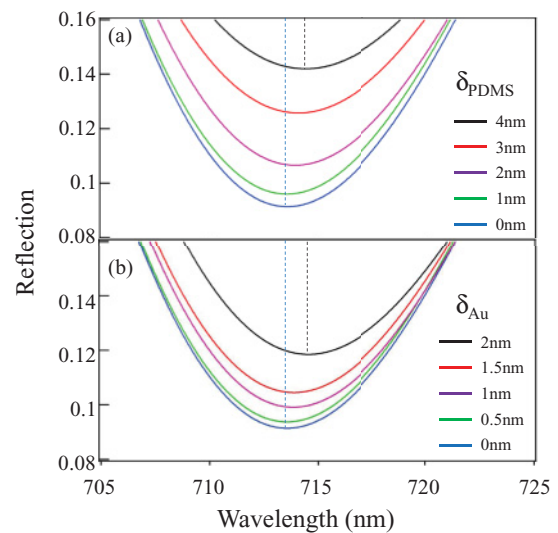
FIG. 6. (Color online) (a) Effect of polymer disorder on first miniband mode for four bilayers; PP fit (blue), disorder of 1 (green), 2 (purple), 3 (red), and 4 nm (black). (b) Effect of metal disorder; PP fit (blue), disorder of 0.5 (green), 1 (purple), 1.5 (red), and 2 nm (black).

layers. Similarly the metal thickness disorder, δ_m, is varied between 0.5 and 2 nm [see Fig. 4(b)]. Again, a reduction in Q is observed, however, the effect is less pronounced. Equivalent drops in Q are observed for $\delta_p = 0.5\%$ and $\delta_m = 10\%$, thus giving similar absolute sensitivities to disorder. Considering the MDBR as a series of Fabry-Perot polymer cavities (where the thin gold layers act as the mirrors), the thickness of the gold controls the coupling between each cavity mode. As δ_m increases, the coupling at either side of the cavity differs and this leads to the reduction in the Q factor. The spectra again redshift, and this is attributed to the wavelength dependence of the mode shifting.

Practically, the polymer disorder describes the inherent roughness of spin-coated polymer layers and agrees well with AFM scans of the polymer surface before sample floating. Polymer roughness can typically be optimized to 1–2 nm using spin-coating techniques. Disorder within the 10-nm-thick gold layers is observed to be between 0.5 and 1 nm from AFM scans (averaged over 20 μm^2 lateral areas), arising from the typically granular nature of thin metal films deposited using thermal evaporation. Although such granular films have been shown to exhibit close to bulk optical behavior,[24] surface roughness can also increase interfacial scattering within the structure, leading to losses and further drops in the Q factor of the miniband modes.

IV. OPTICAL FIELD DISTRIBUTION

By mapping the optical field distributions within the multilayer at several specific frequencies, these optical resonances can be better understood (see Fig. 7). At the foot of the stopband, $\lambda = 470$ nm [see Fig. 7(b)(i)], the optical field resides heavily within the gold layers. The field intensity is seen to drop across each gold layer (vertical lines), and reflection and transmission is minimized. Additionally, as the plasma frequency of gold is approached ($\lambda_p = 520$ nm), resonant absorption occurs within the gold layers, leading to the asymmetrical shape of the stopband. At the summit of the stopband (ii), the field is localized exclusively within the polymer layers leading to very low absorption. Light is

resonantly reflected at this wavelength with contributions from each polymer/gold interface adding constructively to minimise absorption and transmission. The first peak of the transmission miniband (iii) displays high transmission due to the π relative phase change of the incident wave envelope. A full wave envelope sits within the structure and light is able to resonantly tunnel through the gold layers. Absorption is higher at this wavelength than the primary Bloch mode since the optical field has more contact with the gold layers but despite this, 36% transmission is observed. For comparison, 100 nm of equivalent bulk Au transmits only a fraction (10^{-5}) at this wavelength.

The $1/e$ drop-off depth of the field is shown in Fig. 7(c) across the entire width of the stopband. There are two competing effects to the drop-off depth as the wavelength is increased: the resonant absorption of gold around the plasma frequency and the strongly increasing reflection from the periodic spacing of the gold slices. Initially (450–500 nm), the drop-off depth rises as the field begins to move away from the vicinity of the gold layers. However, approaching the plasma frequency of gold, the penetration begins to decrease again due to the resonant interband transitions within the gold layers. The penetration increases sharply moving to longer λ as interband transitions become nonresonant and the Fabry-Perot resonance condition is approached, leading to greatly increased reflection. This depth controls the extent to which injected light probes the structure and is able to deposit energy within each metal layer.[8]

V. FABRY-PEROT MODE DISPERSION

A motorized goniometer with a white-light laser source focused to a 100 μm spot is used to capture reflection spectra across a range of angles in the visible and NIR, and these are shown in Fig. 8 (experiment and simulation) for 4, 6, and 12 bilayers. Calibration of the goniometer ensures optimum sample flatness and axial alignment. Spectra are taken at 0–60° incidence and referenced against a silver mirror. The resulting plots demonstrate the characteristic dispersion of the Bragg modes, their energy increasing with incident angle θ.
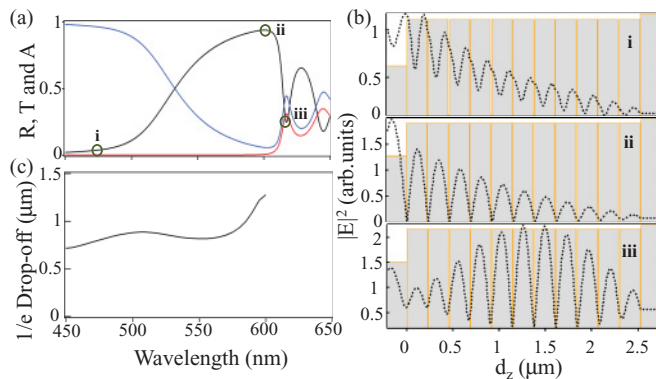

FIG. 7. (Color online) Simulated spectra showing reflection (black), transmission (red), and absorption (blue), for ten-layer structure with (a) 10 nm Au, and (b) E field distribution at (i) plasma frequency, (ii) peak of reflection stopband, and (iii) first Bragg resonance. (c) $1/e$ drop-off of field intensity at different points across stopband.
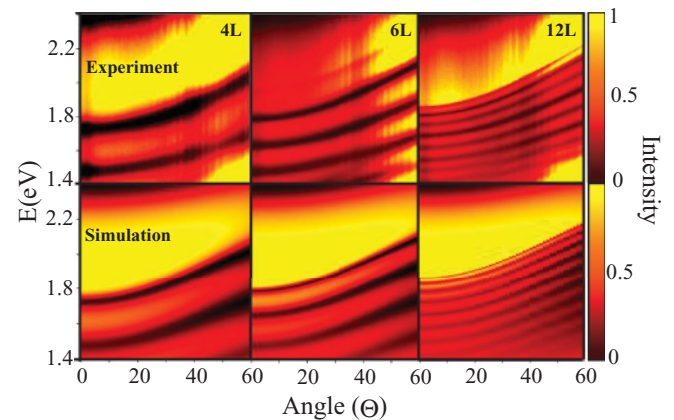

FIG. 8. (Color online) TM-polarized angular-resolved spectra taken at 0–60° incidence for 4, 8, and 12 bilayers and simulations of corresponding multilayers.
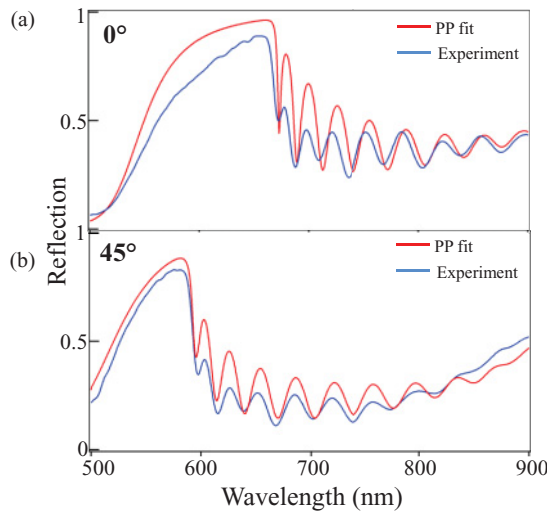
FIG. 9. (Color online) (a) Experimental (blue) and simulated (red) spectral cross sections of 12 bilayers at 0°. (b) Spectral cross sections at 45°.

FIG. 11. (Color online) (a) Angular-resolved visible/NIR spectra of a 12-bilayer sample with TM- (left) and TE-polarized (right) light. The first optical mode is blue shifted by 100 meV at 60° with TE-polarized light. (b) Transfer matrix simulations of corresponding multilayers predict similar results.

Experimental and simulated cross sections from this data set are shown for 12 bilayers at 0° [see Fig. 9(a)] and 45° [see Fig. 9(b)]. The theory accounts well for the expected shift in the miniband Bloch mode positions and shapes. The evolution in Q for the first miniband mode with θ is shown in Fig. 10. Extractions of the experimental data (+) are contrasted with simulations (dashed) for two different samples with six bilayers (red) and ten bilayers (blue). The Q of the mode decreases with angle in both cases as predicted; although the energy of the mode increases, its width also increases, leading to an overall drop in Q. Experimental data display a slightly lower Q than predicted by simulations and this is due to disorder within the layers as discussed above (see Figs. 4–6).

These angular-resolved measurements are repeated with TE-polarized light and contrasted with the TM-polarized

spectra in Fig. 11. An anisotropic energy splitting of the Bloch modes is observed between TE and TM polarizations that increases with θ. This effect arises due to the orientation of the electric field in the reflections from the metal/polymer interfaces. The E field of the TE-polarized light remains parallel to the metal layers throughout rotation while the E field of TM-polarized light rotates with respect to the plane of the layers. This leads to a variation in the penetration depth inside the structures between TM and TE polarizations: the penetration depth increases with θ for TM-polarized light and decreases with θ for TE-polarized light.[32] The energy splitting between TM and TE thus varies with $\sin^2(\theta)$, as shown in Fig. 12 for both experiment (blue) and simulations (red). We note again the reduced splitting in experiment, arising from the effects of disorder in the layers.
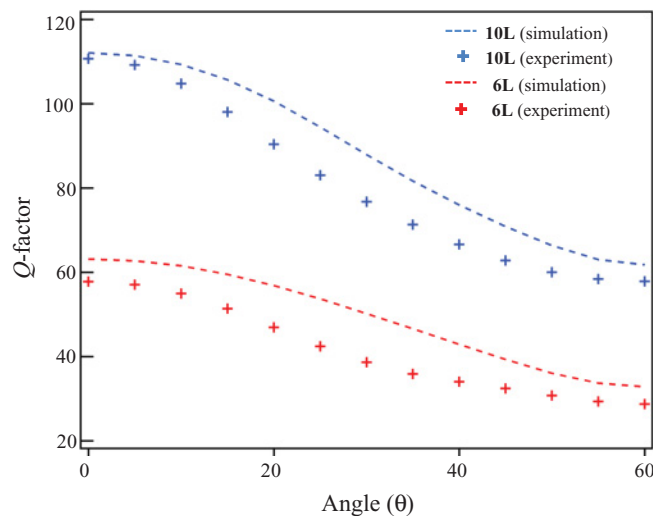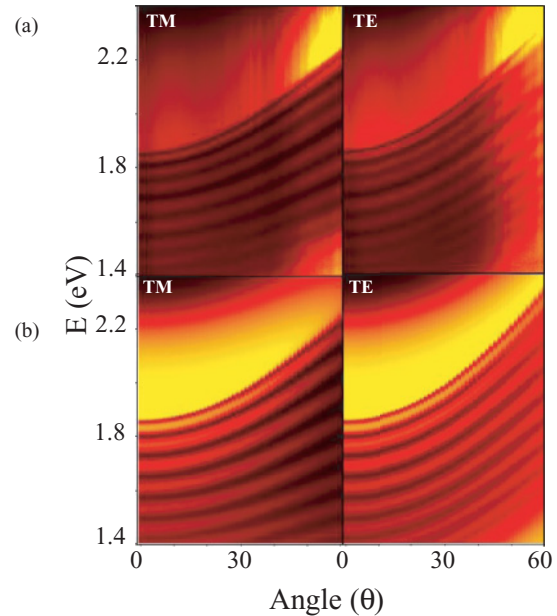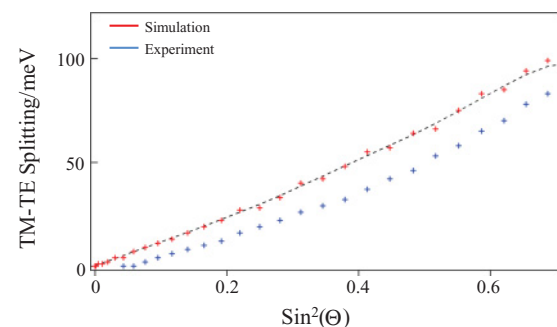

FIG. 10. (Color online) Extracted experimental (+) and simulated (dashed lines) Q of first optical mode with six (red) and ten (blue) bilayers, between 0 and 60°.

FIG. 12. (Color online) TM-TE polarization splitting of first miniband mode for 12 bilayers. Simulation (red) and experiment (blue).

VI. METAMATERIAL CONFIGURATION

Our fabrication method allows for extremely flexible control over layer thickness and alternative configurations are possible. We have demonstrated the optical properties of such metallodielectric multilayers in a Bragg regime however by scaling down the dielectric spacer layers it is possible to enter a metamaterial regime where both layers are now sufficiently thin for the structure to be considered an effective medium.[16] This occurs when $t_{PDMS} \approx t_{Au}$. The effect of this scaling down is to change the coupling between the Fabry-Perot (FP) and surface plasmon (SP) modes, whose coupling is modified by shrinking the dielectric layers.

Simulations of the scaled-down metamaterial structures in Fig. 13 show the effect of reducing the spacing on the development of these modes. The Bragg-arranged configuration with 220-nm PDMS and 18-nm Au [see Fig. 13(a)] displays two minibands, in both the visible and the NIR regions, with the number of FP_i or Bloch modes related to the number of bilayers within the stack, as described previously. Also apparent is the photonic band gap (PBG) of high reflectivity between the minibands. These FP_i modes cross the total internal reflection (TIR) boundary and approach the polymer light line as the field is increasingly tightly trapped within the polymer layers. At values of in-plane momentum, k, beyond the TIR line, guided surface plasmon (SP_i) modes appear.[25] These also form a separate miniband since individual SPs on each thin metal layer couple to each other through their exponentially decaying fields, hence forming $N = L - 1$ coupled SP_i modes. The fields in neighboring SP modes can couple either in-phase or out-of-phase: modes with mostly in-phase coupling have larger fields in the polymer and less in the Au, and hence fall closer to the polymer light line, while modes with mostly out-of-phase coupling have largest field inside the metals, having largest k and largest loss. The origin of these SP_i modes is thus in the symmetric and asymmetric SP modes found on a single thin metal film. Typical field distributions of these modes are plotted in Fig. 14, which shows their relationship with the cavity-confined minibands usually seen in dielectric multiple cavity structures. In such plasmonic minibands, the SPs can thus be continuously tuned from those of the bulk plasmon, to plasmons equivalent to those on impractically thin metal layers.

These FP and SP minibands are clearly seen to be coupled in the Bragg-arranged MDBR structures of Fig. 13(a). The lowest FP_1 mode has the same symmetry as the highest SP_6 mode, and their anticrossing produces a mode splitting of 180 meV. The symmetry of these modes (see Fig. 15) shows the progression from cavity-like modes [see Fig. 15(a)] to plasmonlike modes [see Fig. 15(c)], which both have all the neighboring basis states in antiphase. The other (fully in-phase) configuration goes from cavity-like [see Fig. 15(d)] to plasmonlike [see Fig. 15(f)] through the same anticrossing.

The other modes similarly anticross in pairs from each (SP_i and FP_{7-i}) miniband and as their penetration into the Au layers increases, their splittings become correspondingly
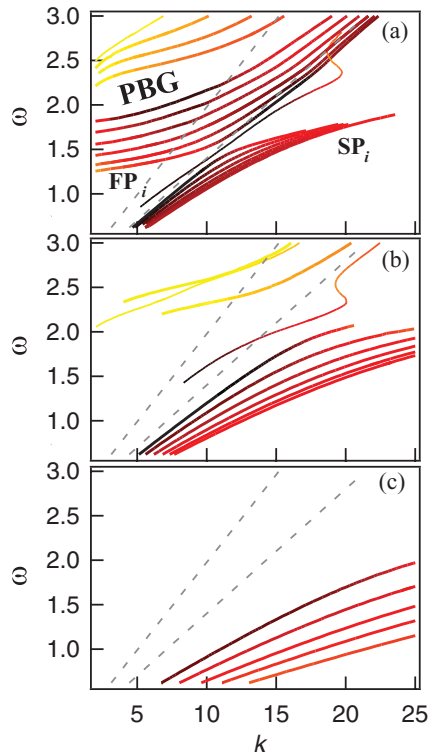

FIG. 13. (Color online) Impedance-method solutions of optical modes within a seven-bilayer structure with 18-nm-thick Au layers spaced by decreasing polymer thickness of (a) 220, (b) 70, and (c) 18 nm. Solutions are shown by lines, with color given by imaginary in-plane k (black to yellow is low to high losses). Light lines for air and PDMS are shown dashed. Six coupled plasmon modes (SP_i) and six coupled Bloch or Fabry-Perot modes (FP_i) are seen in (a).
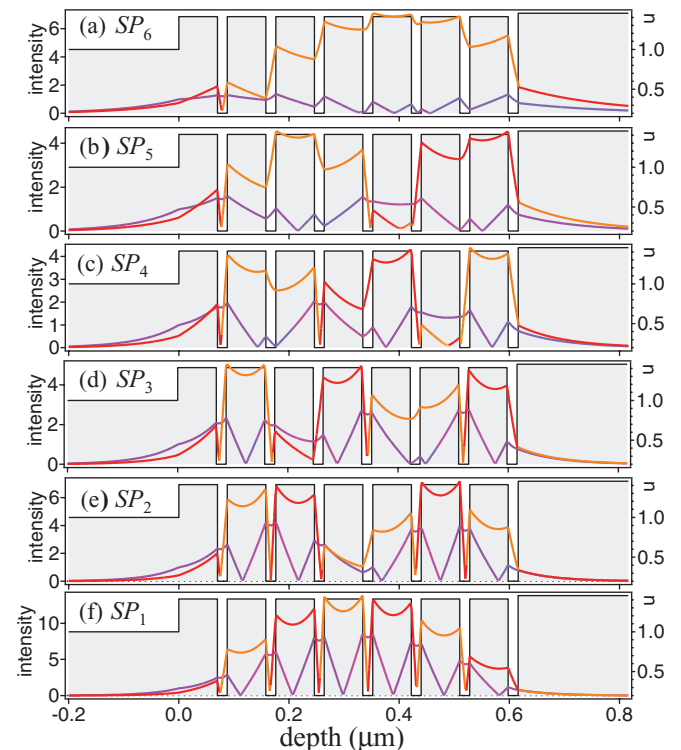

FIG. 14. (Color online) Optical E_z (red) and H_z (purple) fields in a seven-bilayer structure with 70-nm PDMS spacers [of Fig. 13(b)], for the miniband SP_i modes as labeled, at an energy of 1.5 eV, from low to high k (a)–(f).
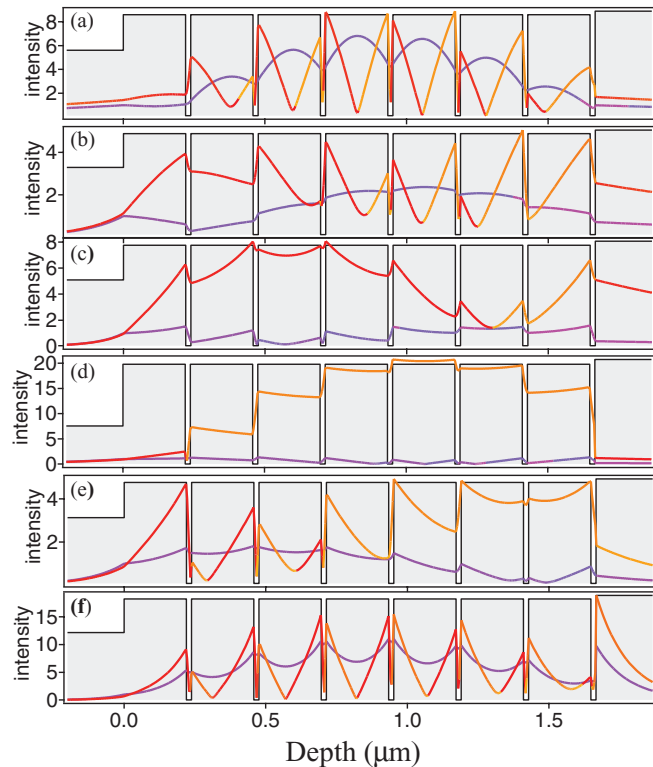
FIG. 15. (Color online) Optical E_z (red) and H_z (purple) fields in a seven-bilayer structure with 220-nm PDMS spacers [of Fig. 13(a)], for (a)–(c), the miniband FP$_1$ modes with $k =$ (a) 5.0, (b) 10.6, and (c) 15.0 μm^{-1}. Equivalent field distributions for the SP$_6$ mode are also shown (d)–(f).

larger. As the modes approach the energy of the 2D surface plasmon of the Au around 2.0 eV, their loss rapidly increases and they disappear. A final additional mode is observed from the broken symmetry of the structure (the extra polymer layer on the surface, and the effect of the substrate), plotted as a thin line in Fig. 13. This mode arises from the spoof plasmon formed by the MDBR, and is tied to the front Au surface at low energies [see Fig. 16(a)] and the substrate surface at high energies [see Fig. 16(b)].

The SP$_i$ minibands act as coupled waveguide modes. As their separation reduces into the metamaterial regime [see Fig. 15(c)], all the FP modes are blue shifted out of view, leaving the SP miniband as the sole way that light can couple
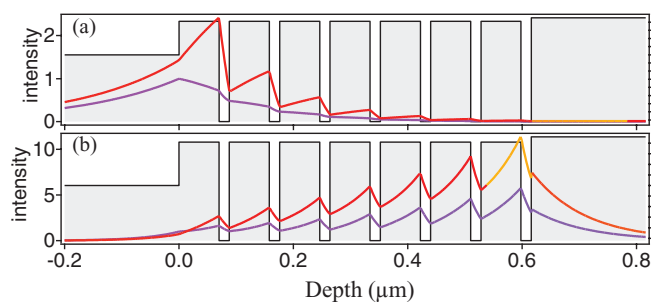

FIG. 16. (Color online) Optical E_z (red) and H_z (purple) fields in a seven-bilayer structure with 70-nm PDMS spacers [of Fig. 13(a)] for the effective SP mode at (a) 1.6 and (b) 2.3 eV.
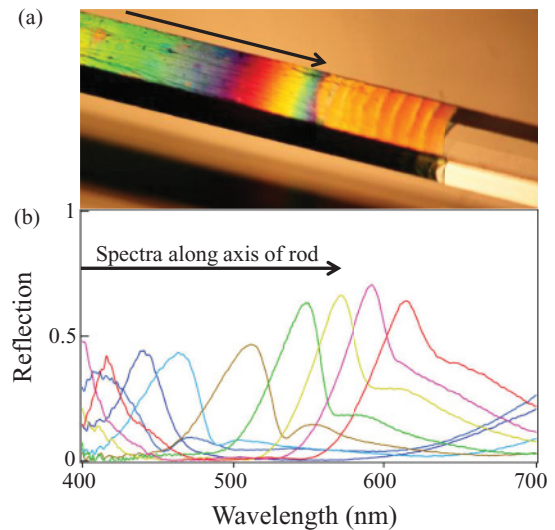

FIG. 17. (Color online) (a) Image of chirped MDBR roll. (b) Corresponding reflection spectra at different positions along the rod axis.

through the structure. Excitation from the far field shows the high reflectivity expected from a 126-nm total thickness of Au. But near-field excitation couples to the SP$_i$ miniband allowing high-k light to penetrate the MDBR. As the number of SP modes increases, a quasicontinuum is formed that couples the near field from one side of the MDBR to the other. Increasing the Au thickness (not shown), reduces the coupling between neighboring plasmons, thus decreasing the splitting between the SP$_i$ modes.

In order to couple to these modes from the far field, interfacial scattering, diffraction, or evanescent methods must be used. Two new possibilities are offered by the current cylindrical roll geometry. By slicing the structure normal to the roll, direct edge coupling to these SP$_i$ states is possible, however, the high losses mean that submillimeter lengths have to be sectioned to detect light on the far side. Another possibility is to engineer corrugations within the layers for direct diffractive coupling. We have recently succeeded in fabricating such grating multilayers in the Bragg regime with larger pitches.[28] To couple to the plasmon modes in this way requires a subwavelength grating, $\Lambda \approx 40$ nm, where Λ is the grating pitch. Gratings of this dimension can be fabricated with e-beam or template lithography,[27] and this scaledown is in progress. Coupling to the multiple SPP modes is of interest for nonlinear interactions and optical Bloch oscillations.

Finally, we demonstrate the capability to provide chirped metallodielectric stacks (see Fig. 17). As discussed above,[13] by introducing an optical thickness gradient across the superlattice cavity layers, their photonic bands can be tilted, leading to photonic Bloch oscillations and Zener tunneling of light waves. Using our RRA fabrication method, this can be achieved by engineering a thickness gradient in the polymer component of the initial bilayer (for instance, by using doctor-blade coating at variable speed). The film is then rolled-up parallel to this gradient. We have achieved such graded polymer layers by tilted blade coating (see Fig. 17) and by large area spin coating (which introduces a continuous thickness gradient from the edge to the center of the film).

VII. CONCLUSIONS

We demonstrate and discuss the optical properties of metallodielectric multilayers, both in a Fabry-Perot configuration (MDBR) and a subwavelength metamaterial configuration. The spectral response of the MDBRs is well accounted for by both a simple model based on minibands as well as detailed impedance method simulations of the optical field distribution within the stack. The dispersion of these Bloch modes is analyzed, and the influence of roughness on the Q factors, tuning, and resonant line shapes is identified. In the metamaterial configurations, trapped plasmon modes are found on reducing the dielectric spacer thickness. This configuration can lead to plasmonic coupling and negative refraction,[15] as has been demonstrated with optical hyperlensing.[18]

An appealing aspect of the fabrication method is the wide range of potential materials and configurations that are available, allowing the optical properties of the multilayer to be tuned. Geometries ranging from square or cylindrical, solid or hollow core, can be produced for lensing applications. Additionally, the substrate can be templated before deposition, leading to patterned multilayers. Rigid, elastomeric, thermoelastic, and other polymers can be used to allow active control of the dielectric layers. While we previously reported purely dielectric stretch-tuneable DBRs and microcavities,[26] this is not possible in a flat geometry with gold. However, corrugated MDBRs can be stretched since the gold layer is able to fold like a concertina within the multilayer. This approach to "stretchable gold" has been well studied with PDMS and gold for digital electronics.[29] Capabilities for extending current approaches for flexible plasmonics[30] and metamaterials,[31] are clearly demonstrated here.

*ng322@cam.ac.uk

[1] E. Yablonovitch, Phys. Rev. Lett. **58**, 2059 (1987).

[2] K. J. Vahala, Nature (London) **424**, 839 (2003).

[3] M. J. Bloemer and M. Scalora, Appl. Phys. Lett. **72**, 1676 (1998).

[4] N. Gibbons, J. J. Baumberg, C. L. Bower, M. Kolle, and U. Steiner, Adv. Mater. **21**, 3933 (2009).

[5] R. S. Bennink et al., Opt. Lett. **24**, 1416 (1999).

[6] N. N. Lepeshkin, A. Schweinsberg, and G. Piredda, Phys. Rev. Lett. **93**, 123902 (2004).

[7] G. Ma and S. H. Tang, Opt. Lett. **32**, 3435 (2007).

[8] Petros Farah, Nicholas Gibbons, Fu Min Huang, and J. J. Baumberg, Phys. Rev. B **84**, 125442 (2011).

[9] M. C. Larciprete, A. Belardini, M. G. Cappeddu, D. deCeglia, M. Centini, E. Fazio, C. Sibilia, M. J. Bloemer, and M. Scalora, Phys. Rev. A **77**, 13809 (2008).

[10] E. Lidorikis, M. M. Sigalas, E. N. Economou, and C. M. Soukoulis, Phys. Rev. Lett. **81**, 1405 (1998).

[11] M. Bayindir, C. Kural, and E. Ozbay, J. Opt. A: Pure Appl. Opt. **3**, S184 (2001).

[12] R. Sapienza, P. Costantino, D. Wiersma, M. Ghulinyan, C. J. Oton, and L. Pavesi, Phys. Rev. Lett. **91**, 263902 (2003).

[13] M. Ghulinyan, C. J. Oton, Z. Gaburro, L. Pavesi, C. Toninelli, and D. S. Wiersm, Phys. Rev. Lett. **94**, 127401 (2005).

[14] J. B. Pendry, Phys. Rev. Lett. **85**, 3966 (2000).

[15] J. B. Pendry and S. A. Ramakrishna, Physica B **338**, 329 (2003).

[16] J. C. M. Garnett, Philos. Trans. R. Soc. London A 237 (1906).

[17] B. Wood, J. B. Pendry, and D. P. Tsai, Phys. Rev. B **74**, 115116 (2006).

[18] N. Fang et al., Science **308**, 534 (2005).

[19] Z. Liu, H. Lee, Y. Xiong, C. Sun, and X. Zhang, Science **315**, 1686 (2007).

[20] Anan Fang, Thomas Koschny, and Costas M. Soukoulis, Phys. Rev. B **79**, 245127 (2009).

[21] M. Scalora et al., Opt. Express **15**, 508 (2007).

[22] M. Mazilu and K. Dholakia, Opt. Express **14**, 7709 (2006).

[23] A. Yariv et al., Opt. Lett. **24**, 711 (1999).

[24] H. Monard and F. Sabary, Thin Solid Films **310**, 265 (1997).

[25] H. Raether, *Surface Plasmons on Smooth and Rough Surfaces and on Gratings* (Springer-Verlag, Berlin, 1988).

[26] M. Kolle, B. Zheng, N. Gibbons, J. J. Baumberg, and U. Steiner, Opt. Express **18**, 4356 (2010).

[27] M. D. Austin et al., Appl. Phys. Lett. **84**, 5299 (2004).

[28] N. Gibbons and J. J. Baumberg, Opt. Express **19**, 15596.

[29] S. P. Lacour, S. Wagner, Z. Huang, and Z. Suo, Appl. Phys. Lett. **82**, 2404 (2003).

[30] F. Huang, J. J. Baumberg, Nano Lett. **10**, 1787 (2010).

[31] I. M. Pryce, K. Aydin, Y. A. Kelaita, R. M. Briggs, and H. A. Atwater, Nano Lett. **10**, 4222 (2010).

[32] G. Panzarini, L. C. Andreani, A. Armitage, D. Baxter, M. S. Skolnick, V. N. Astratov, J. S. Roberts, A. V. Kavokin, M. R. Vladimirova, and M. A. Kaliteevski, Phys. Rev. B **59**, 5082 (1999).